The Effect of Powder Size and Morphology on the Sinterability of Bioresorbable Mg-Sr/Ca Alloys

Ava Azadi[1*], Eoin D. O'Cearbhaill[1] and Mert Celikin[1]

[1]School of Mechanical and Materials Engineering, University College Dublin, Ireland

[*]Corresponding author: ava.azadichegeni@ucdconnect.ie

Keywords: Magnesium (Mg) Alloys, Alloy Design, Thermodynamic Calculations, Materials Characterisation, Sintering

Abstract

Possessing outstanding biocompatibility and bioresorbability, magnesium (Mg) alloys with strontium (Sr) and calcium (Ca) additions have shown potential to be used as temporary implants in orthopaedic applications. Having a low elastic modulus (45 GPa) close to the human bone lowers the stress shielding effects. Low temperature Additive Manufacturing (AM) techniques (e.g., Fused Deposition Modelling) have potential to be used for the fabrication of complex Mg components while avoiding safety concerns associated with high temperature AM. However, low sinterability of common Mg-alloys is the main limiting factor. The objective of this work is to investigate the effect of powder particle size / morphology on the sinterability of Mg-Ca/Sr based alloys produced via powder metallurgy. Laser Diffraction and Scanning Electron Microscopy (SEM) were used to characterize particle size and morphology. The study also focused on assessing the role of liquid phase sintering (LPS) mechanism by thermodynamic calculations and microstructural characterisation (SEM). Porosity measurements using density analysis and image processing were employed to determine the effects of powder size and morphology on sinterability of the alloys. It was found that the non-homogeneous particle size distribution with more spherical powder particles, facilitated the compaction and accordingly higher densification was obtained. This was achieved for powders milled at higher speeds (900 rpm), resulting in significantly lower porosity levels (~ 6-8 %) compared to the dry-milled state (~ 40-60 %).

1. Introduction

Magnesium (Mg) and its alloys have been receiving increased attention as emerging class of biomedical alloys due to their bioresorbability and biocompatibility [1, 2]. As temporary implants, they have proven high potentials in orthopaedic and cardiovascular applications, eliminating the need for the secondary surgical operations commonly conducted for conventional non-resorbable implants [3, 4]. Furthermore, the use of bioresorbable Mg implants decreases the risk of stress shielding effects thanks to the relatively low elastic modulus of Mg alloys (45 GPa) that is comparable to the human bone (1-30 GPa) [3–7]. However, current manufacturing processes have limitations for the customisation of Mg-based implants based on patients' requirements [8, 9].

Additive manufacturing (AM) of Mg-based alloys enables fast production of personalised implants with intricate designs, expanding the potential of Mg-based alloys for biomedical applications [10–12]. High temperature AM techniques such as laser powder bed fusion (LPBF) have been commonly used for Mg AM [13, 14]. However, safety concerns typically

arise during the processing of Mg-based alloys via high temperature AM methods due to the inherent limitations of Mg, including low boiling temperature and high vapor pressure [15, 16]. Additionally, the chemical composition of the Mg-based alloys might undergo changes due to the temperature evolution exceeding the evaporation point of Mg [17, 18]. Hence, low temperature AM techniques such as fused filament fabrication (FFF) and binder jetting (BJ) are more compatible with the intrinsic properties of Mg-based alloys. However, one of the main challenges of low temperature Mg alloy AM is the low sinterability of the current Mg-based alloys, restricting the printability of Mg using FFF and BJ techniques [19–21]. Since Mg powder has high affinity for oxygen and upon exposure to air a stable oxide layer (i.e., MgO) is formed on the powder surface which has no solubility in solid Mg, acting as diffusion barrier during sintering [21, 22]. Therefore, liquid phase sintering (LPS) can be employed to improve Mg sinterability as the capillary force of the liquid phase causes the powder particles to come together. However, sintering of Mg is still challenging. [23–25].

The aim of this study is to enhance the sinterability of Mg-Sr/Ca based alloys by understanding the effect of powder size distribution and morphology. The study will focus on optimising Liquid Phase Sintering (LPS) mechanism supported by thermodynamic calculations.

2. Experimental Procedure

Two binary alloys with nominal compositions of Mg-20Ca and Mg-20Sr (in weight %) were studied using the commercial master alloys supplied by Shanghai Xinglu Chemical Tech. China Company. Inductively coupled plasma (ICP) analysis was used to determine the chemical compositions of the cast ingots (Table 1). Therefore, the actual compositions are Mg-18.2Ca and Mg-20.9Sr.

Table 1. ICP analysis of alloy compositions, (wt.%)

Alloy	Sr	Ca	Mg
Mg-20Ca	0.01	18.24	bal.
Mg-20Sr	20.91	0.01	bal.

The commercial ingots were dry milled in order to fabricate the starting material in the form of powder particles using slow speed Emill milling machine with following parameters: depth of cut 1mm, length of travel 200mm per minute, without lubricant. Afterwards, the dry-milled particles were ball milled in a vertical lab planetary ball milling equipment (DECO-PBM-V-0.4L) using stainless steel jars and 10 mm balls under argon (Ar) gas. The ball-milling variables are duration, ball-to-powder ratio (BPR), and speed, and accordingly 3 conditions were defined per composition; duration effect, BPR effect and speed effect, respectively (Table 2).

Table 2. Ball milling parameters and conditions.

BPR	Speed (rpm)	Time (h)	Condition
10:01	650	1	Duration Effect
		4	
14:01	650	1	BPR Effect
		4	
10:01	900	1	Speed Effect
		4	

To investigate the effect of ball-milling variables on sinterability of the alloys, the powder size distribution and morphology of each ball milling condition was evaluated using Microtrac MRB TurboSync particle analyser laser diffractometer. Approximately 2 g of ball-milled powders were used to fabricate discs of Mg-18.2Ca and Mg-20.9Sr compositions in a circular die with a diameter of 25 mm, using cold pressing set-up (PA 260, Josef Lucas LTD Birmingham) under applied pressure of 60 bar and dwell time of 2.5 min. In order to determine the appropriate temperature range for sintering in terms of liquid phase fraction, thermodynamic calculations were performed on both compositions using ThermoCalc software package (TCMG6 Mg-Alloys v6.3 database). In addition, differential scanning calorimetry (DSC) was conducted on Mg-18.2Ca and Mg-20.9Sr ball-milled powders using STA 1500 Rheometric Scientific equipment with the following profile: heating at 5 °C/min from ambient temperature to 700 °C under Ar gas. Sintering was performed on discs of Mg-18.2Ca and Mg-20.9Sr in a tube furnace (Lenton Tube Furnace 1600) in a controlled atmosphere of Ar from room temperature (RT) with heating rate of 5 °C/min to 575 °C/min, dwell time of 2 h and subsequent furnace cooling to the ambient temperature. Cross sections of sintered discs were cut and metallographically prepared following the standard procedure down to 1μm diamond paste polishing step, and along with the ball-milled powders of both compositions were examined under scanning electron microscope (SEM) using TM4000Plus Tabletop Hitachi, Japan setup. To measure the densification of the sintered parts, image analysis was employed using MATLAB software package. In addition, density measurements were conducted based on Archimedes principle in ethanol medium.

3. Results and Discussion

3.1. Powder Fabrication and Characterisation

SEM micrographs of the dry-milled Mg-18.2Ca and Mg-20.9Sr particles are shown in Figure 1. Dry milling of cast ingots was the initial step of powder fabrication for both compositions. It is observed that the dry-milled particles exhibit sharp edges with irregular morphologies varying from μm to mm ranges in size. For more accurate analysis, size distribution of the dry-milled particles was studied, and D10, D50 and D90 values of the dry-milled particles are reported in Table 3, where Dx is defined as the size of X% of the particles being below a measured quantity. Both compositions have almost the same D50 value (50% of the particles have a particle size equal to or smaller than ~ 367 μm). However, particle size variation is more conspicuous for Mg-20.9Sr alloy with D10 of 44.39 μm and D90 of 1120 μm.

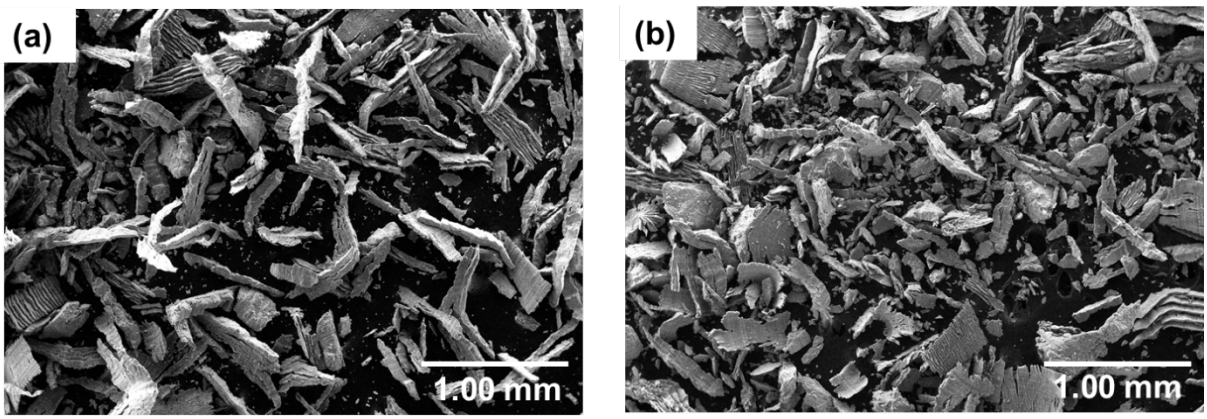

Figure 1. SEM micrographs of dry-milled particles of (a) Mg-18.2Ca and (b) Mg-20.9Sr alloys showing the initial state of the produced particles.

Table 3. Laser diffraction (LD) results representing the size distribution of dry-milled particles.

Composition	D10	D50	D90
Mg-20.9Sr	44.39	366.5	1120
Mg-18.2Ca	116.9	367	672.2

Figures 2 and 3 represent the SEM micrographs of dry-milled particles of Mg-18.2Ca and Mg-20.9Sr, respectively, after 1 h and 4 h of ball-milling. It can be seen that after 1 h ball milling, the large, dry-milled particles (Figure 1) of all conditions significantly reduced in size. Moreover, regardless of the conditions, the longer ball milling duration (i.e., 4 h) resulted in the finer particles for both compositions. Starting with Mg-18.2Ca composition, after 1h of ball milling, it is determined that the speed increase (i.e., from 650 rpm 900rpm) led to finer particles compared to the results of Duration and BPR Effects. Even after further 3 hours of ball milling, the particles produced at higher speeds (900 rpm) became finer than those produced by Duration and BPR Effects. Furthermore, it can be asserted that the results of Duration and BPR variables are comparable. Similar trend can be observed for Mg-20.9Sr composition in terms of Duration and BPR Effects. However, it seems that the speed increase led to the agglomeration of the particles in Mg-20.9Sr composition; after 1 h ball milling the largest particles are correspond to the Speed Effect among all 3 conditions.

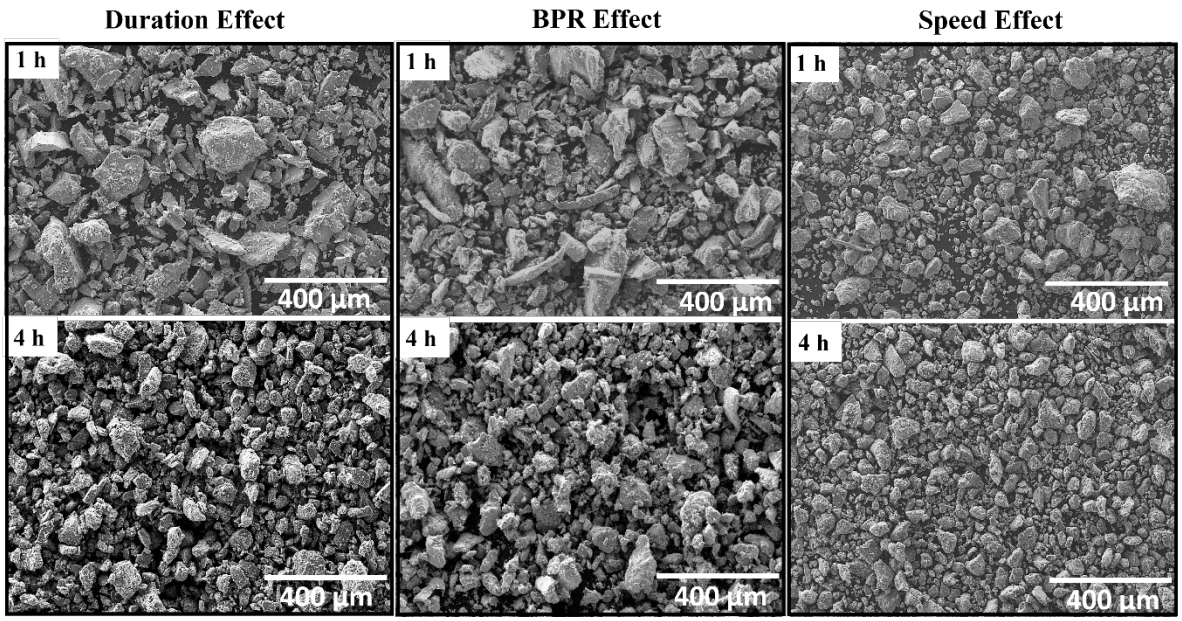

Figure 2. SEM micrographs of Mg-18.2Ca after ball milling.

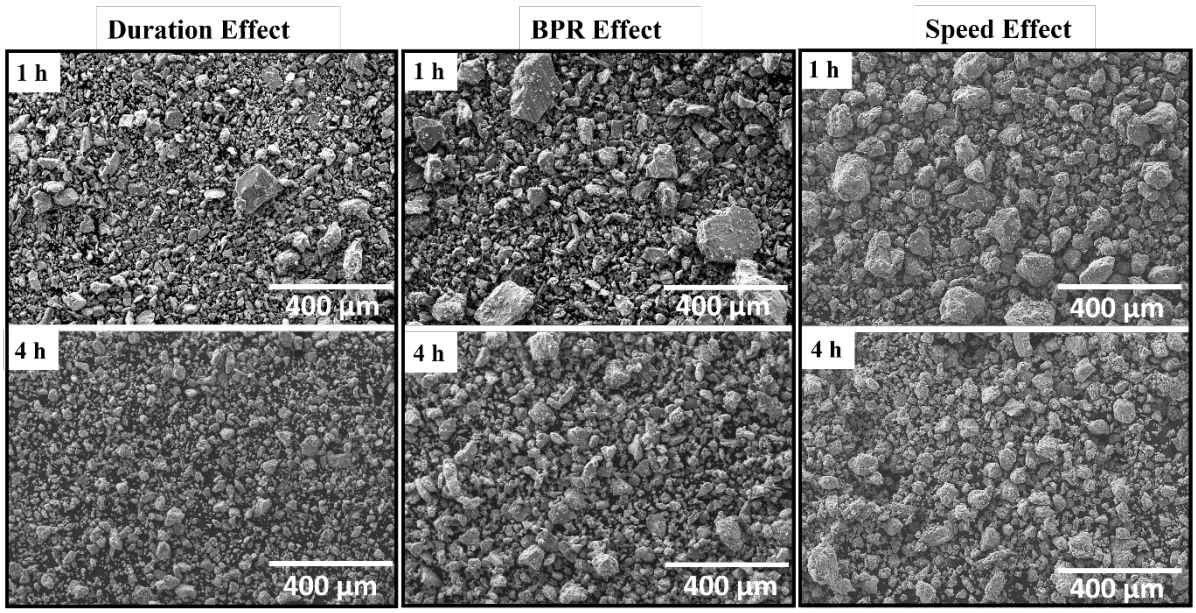

Figure 3. SEM micrographs of Mg-20.9Sr after ball milling.

Size distribution of ball-milled Mg-18.2Ca and Mg-20.9Sr powder particles is summarised in Table 4. Generally, the quantitative size distribution values are in good agreement with the SEM micrographs for both compositions, confirming that the size of powders produced by BPR and Duration Effects are comparable, and there is not a remarkable difference between the resultant values. However, D10 and D50 values of Mg-20.9Sr powder particles are smaller than those of Mg-18.2Ca, considering the Duration and BPR Effects, whileD90 values of Mg-20.9Sr are larger than those of Mg-18.2Ca. Mg-20.9Sr powder particles have a bimodal size distribution which might be due to the agglomeration of the particles during ball milling or due to the higher oxygen content during powder processing. In addition, the laser diffraction technique is sensitive to outlier particles and the possible inclusion of a few large particles (as particles were not sieved before ball milling) affect D90 values.

Table 4. Laser diffraction results representing the size distribution of ball-milled particles.

Composition	Condition	D10	D50	D90
Mg-18.2Ca	Duration Effect	43.81	92.18	207.30
	BPR Effect	40.95	89.76	264.80
	Speed Effect	17.89	56.44	351.53
Mg-20.9Sr	Duration Effect	21.48	61.82	261.60
	BPR Effect	27.83	73.73	312.40
	Speed Effect	6.60	29.21	214.20

Morphological transformation can be readily perceived comparing the SEM micrographs in Figures 1-3. The sharp-edged particles of both compositions became more spherical after 1 h and 4 h of ball milling. Sphericity is a measure of the degree to which a particle approximates the shape of a perfect sphere, and it has a value of 1 representing a perfect sphere and 0 representing a totally non-spherical particle [26]. The sphericity indices (SI) of dry-milled and ball-milled particles are shown in Figure 4. The mean SI of dry-milled particles are 0.522 and 0.504, corresponding to Mg-18.2Ca and Mg-20.9Sr, respectively. After ball milling, the average SI increased to 0.88 for both compositions, implying that the ball-milled particles became closer to the morphology of a sphere.

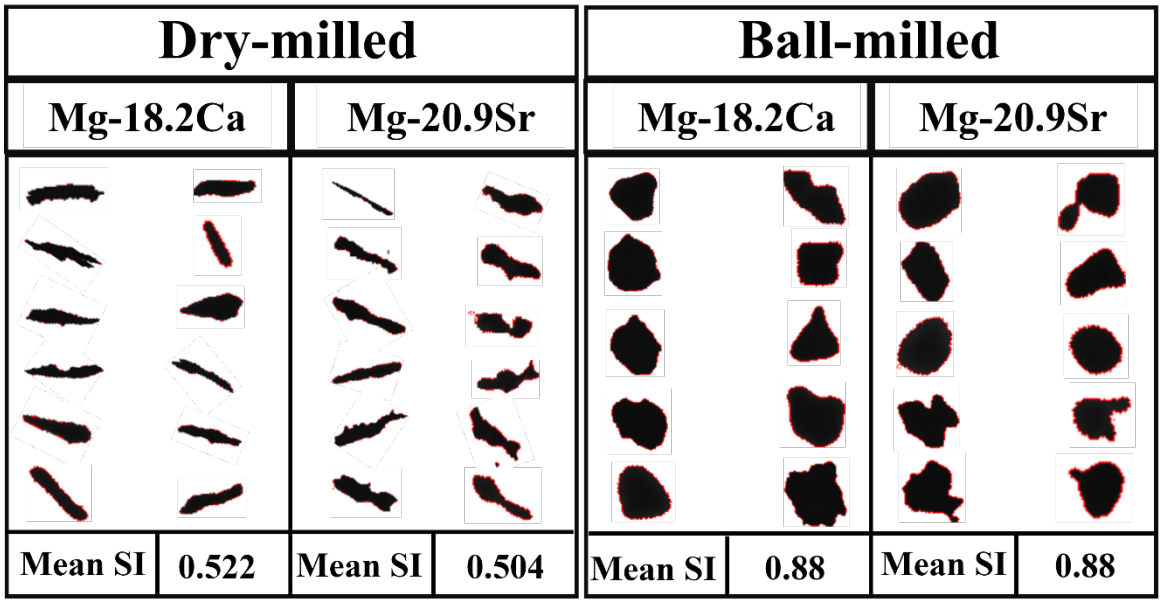

Figure 4. Sphericity index results obtained by laser diffraction technique.

3.2. Sinterability Evaluation

Liquid phase fraction diagrams of Mg-Ca and Mg-Sr systems are illustrated in Figure 5. The theoretical liquidus and solidus temperatures of Mg-Ca system are 572.3 °C, and 518.27 °C, respectively, and 593.17 °C and 588.25 °C, respectively for Mg-Sr system. It can be seen that Mg-Sr system has a relatively narrower solidification temperature range compared to Mg-18.2Ca. The liquid phase volume fraction was calculated for both compositions. Theoretically,

it can be seen that at 570 °C, Mg-18.2Ca system is approximately in fully liquid state while no liquid is expected in Mg-20.9Sr system.

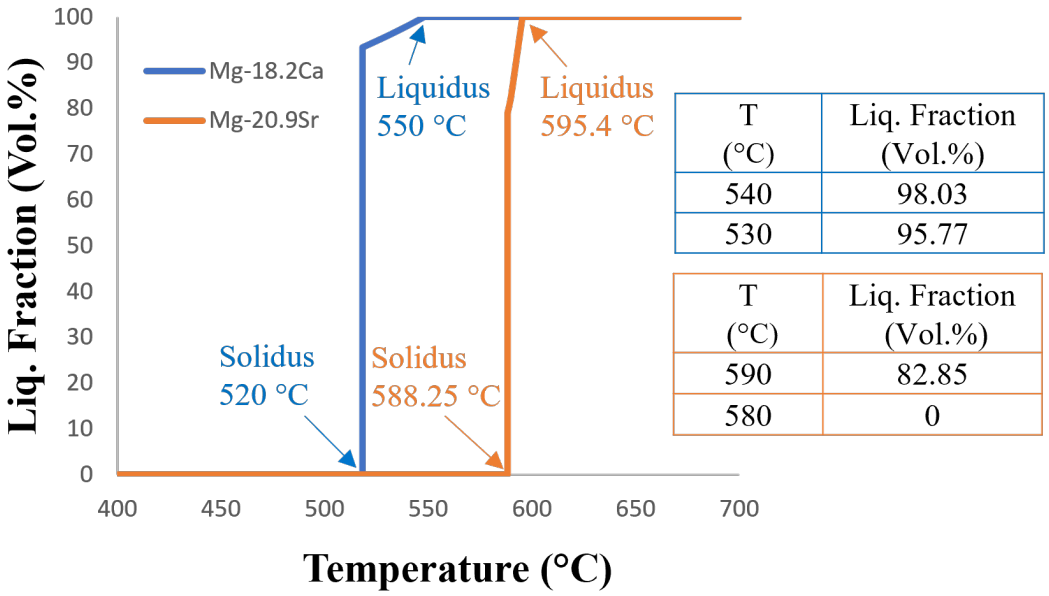

Figure 5. Liquid volume fraction curves of Mg-18.2Ca and Mg-20.9Sr.

DSC curves of Mg-18.2Ca and Mg-20.9Sr alloys are presented in Figure 6. In Mg-18.2Ca system, there is an endothermic peak in the temperature interval of 464-544 °C, with a minimum of 520.24 °C. The peak onset which represents the solidus, occurs at 464.17 °C, and the endset temperature representing the liquidus, occurs at 544.55 °C. In addition, in Mg-20.9Sr system, the endothermic peak appears in temperature interval of 556-590 °C, with a minimum at 582.55 °C. Therefore, the solidus of this system is determined as 556.17 °C, and the liquidus is 590.05 °C. Comparing the theoretical values obtained from the thermodynamic calculations (Figure 5) and DSC results, the main reason for the difference in theoretical solidus and liquidus values with those obtained from the thermal analysis originated from the fact that the thermodynamic calculations are based on the data of bulk materials. However, DSC was carried out on the powder particles surrounded by the MgO film. Additionally, the theoretical temperature calculations consider the thermodynamic equilibrium while the thermal analysis is dependent upon the heating rate; with decreasing the heating rate the onset of a transformation shifts to lower temperatures [27]. In accordance with both thermal analysis and thermodynamic calculations, the sintering temperature was selected to be 625 °C for both compositions.

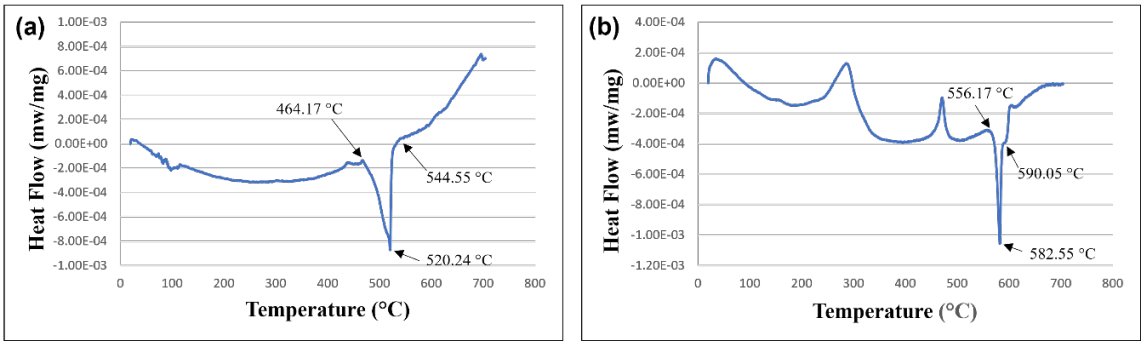

Figure 6. DSC curves of (a) Mg-18.2Ca, and (b) Mg-20.9Sr.

Figure 7 shows the SEM micrographs of the fully dense regions of ball-milled specimens of Mg-18.2Ca and Mg-20.9Sr after sintering. The presence of the liquid phase can be confirmed from the graphs. The lamellar microstructure is an indication of the solidified liquid phase within the microstructure. Unlike the sintering results of the dry-milled specimens of the same compositions previously investigated [28] , the liquid phase formed during sintering at 575°C was maintained within the microstructure, and the structural integrity was preserved. This might be due to the finer size of the particles obtained after ball milling, and accordingly, the ease of compaction with finer powders compared to the dry-milled state. In addition, the liquid phase fills in the pores of the microstructure and thereby reduces the overall porosity level. As can be observed in Figure 7, there is no porosity in the regions where the liquid phase solidified. However, the porosity was found to be in the regions where solid-state sintering is the controlling mechanism and no liquid phase was formed.

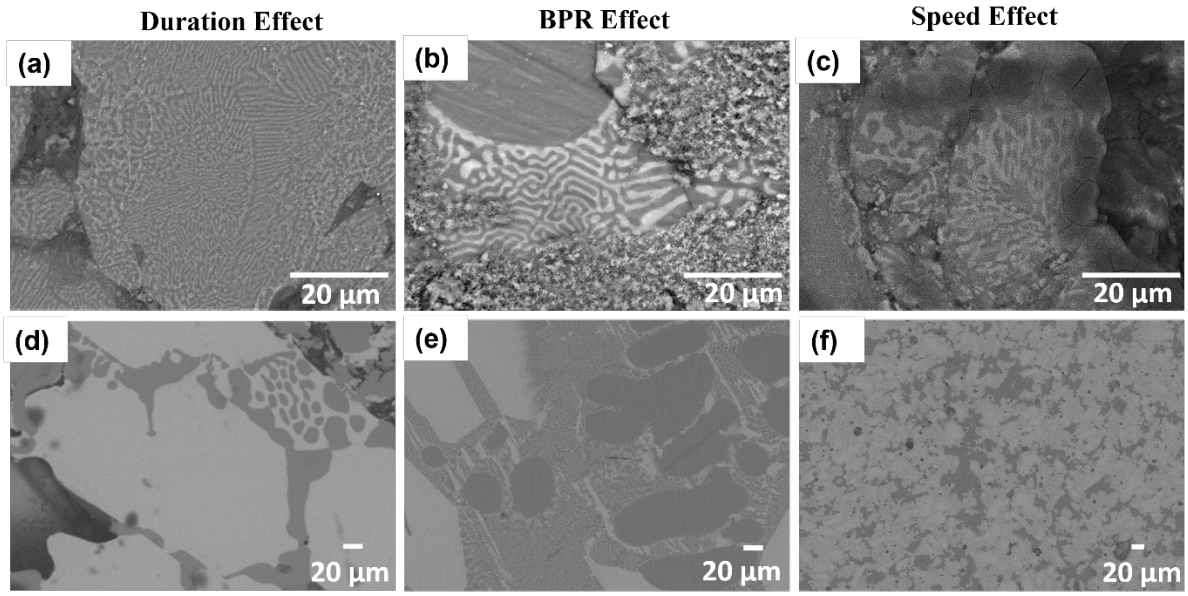

Figure 7. SEM micrographs of (a-c) Mg-18.2Ca, and (d-f) Mg-20.9Sr, indicating the liquid formation during sintering at 575 °C

Porosity measurements were performed on sintered Mg-18.2Ca and Mg-20.9Sr specimens using both image analysis technique (Figure 8a) and Archimedes density method (Figure 8b). Generally, the porosity levels of the ball-milled specimens significantly dropped for both compositions compared to the dry-milled specimens (62.37% and 42.52% correspond to Mg-18.2Ca and Mg-20.9Sr in dry-milled state). In addition, a similar trend applies to both compositions with Speed Effect showing the lowest porosity level (6% and 8% correspond to Mg-18.2Ca and Mg-20.9Sr, respectively), and BPR Effect resulted in the highest porosity level (35% and 41% correspond to Mg-18.2Ca and Mg-20.9Sr, respectively) among 3 ball milling conditions. Furthermore, effects of Duration and BPR are comparable, with Duration Effect being slightly more effective in terms of densification in both compositions (29% and 39% correspond to Mg-18.2Ca and Mg-20.9Sr, respectively).

Archimedes density measurements of both compositions revealed that the porosity level of Mg-18.2Ca specimens substantially decreased to 1.93%, 1.77% and 1.43% correspond to Duration, BPR, and Speed Effects, respectively. In addition, the porosity of Mg-20.9Sr also decreased to 16.07% and 12.69% correspond to Duration and BPR Effects. However, the value of porosity remained unchanged for Speed Effect. On the basis of both density measurements and image

analysis results, it was affirmed that Speed Effect resulted in less porosity levels and therefore, more promising for achieving higher densification. This could be due to the presence of both fine and coarse powder particles which was obtained at higher speeds of ball milling and caused an improved green part compaction which resulted in higher densification.

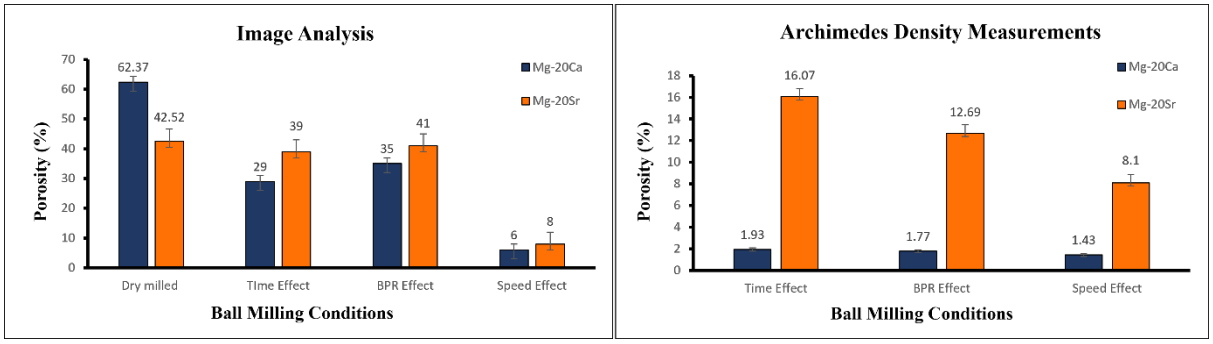

Figure 8. Graphs of porosity measurements using (a) image analysis, and (b) Archimedes density measurements.

Conclusion

This study investigated the sinterability of two binary alloys, namely Mg-18.2Ca and Mg-20.9Sr. Initial powders were fabricated using dry-milling and ball-milling techniques. The impacts of alloying elements (Ca and Sr) were evaluated by thermodynamic calculations and thermal analysis. The effect of ball milling parameters (Duration, BPR and Speed) was also investigated. The following remarks can be derived from this study:

- After ball milling, particle size reduction and morphological transformation were observed; irregular and large dry-milled particles became more spherical and finer.
- Porosity levels of ball-milled specimens decreased compared to the dry-milled results.
- Particle size distributions as a result of Duration Effect and BPR Effect were approximately similar, and porosity levels of both conditions calculated by image analysis were comparable.
- Among ball milling conditions, Speed Effect resulted in non-homogeneous particle size distribution causing higher compaction and higher densification.

Acknowledgements

This project has received funding from the European Union's Horizon 2020 research and innovation programme under the Marie-Sklodowska-Curie grant agreement No 101029651. This publication has also emanated from research conducted with the financial support of Science Foundation Ireland under grant number 20/FFP-P/8868. For the purpose of Open Access, the author has applied a CC BY public copyright licence to any Author Accepted Manuscript version arising from this submission. Authors also thank South Eastern Applied Materials (SEAM) Research Centre for their support in conducting laser diffraction experiments.

References

[1] Jamel MM, Jamel MM, Lopez HF (2022) Designing Advanced Biomedical Biodegradable Mg Alloys: A Review. Metals 12(1):85. https://doi.org/10.3390/met12010085

[2] Sharma SK, Saxena KK, Malik V, Mohammad KA, Prakash C, Buddhi D, Dixit S (2022) Significance of Alloying Elements on the Mechanical Characteristics of Mg-Based

Materials for Biomedical Applications. Cryst. 12(8):1138. https://doi.org/10.3390/cryst12081138
[3] Amukarimi S, Mozafari M (2021) Biodegradable magnesium-based biomaterials: An overview of challenges and opportunities. Med Comm. 2(2):123–144. https://doi.org/10.1002/mco2.59
[4] Zhou H, Liang B, Jiang H, Deng Z, Yu K (2021) Magnesium-based biomaterials as emerging agents for bone repair and regeneration: from mechanism to application. JMA 9(3):779–804. https://doi.org/10.1016/j.jma.2021.03.004
[5] Alam ME, Pal S, Decker R, Ferreri NC, Knezevic M, Beyerlein IJ (2020) Rare-earth- and aluminum-free, high strength dilute magnesium alloy for Biomedical Applications. Sci. Rep. 10(1):15839. https://doi.org/10.1038/s41598-020-72374-z.
[6] Maier P, Hort N (2020) Magnesium Alloys for Biomedical Applications. Metals 10(10):1328. https://doi.org/10.3390/met10101328
[7] Yang Y, He C, Dianyu E, Yang W, Qi F, Xie D, Shen L, Peng S, Shuai C (2020) Mg bone implant: Features, developments and perspectives. Mater. Des 185:108259. https://doi.org/10.1016/j.matdes.2019.108259
[8] Zamani Y, Ghazanfari H, Erabi G, Moghanian A, Fakic B, Hosseini SM, Mohammad BP(2021) A review of additive manufacturing of Mg-based alloys and composite implants. JCC 2(5):71–83. https://doi.org/10.52547/jcc.3.1.7
[9] Kuah KX, Blackwood DJ, Ong WK, Salehi M, Seet HL, Nai MLS, Wijesinghe S (2022) Analysis of the corrosion performance of binder jet additive manufactured magnesium alloys for biomedical applications. JMA 10:1296-1310. https://doi.org/10.1016/j.jma.2021.11.016
[10] Zeng Z, Salehi M, Kopp A, Xu S, Esmaily M, Birbilis N (2022) Recent progress and perspectives in additive manufacturing of magnesium alloys. JMA 10(6):1511-1541. https://doi.org/10.1016/j.jma.2022.03.001
[11] Allavikutty R, Gupta P, Santra TS, Rengaswamy J (2021) Additive manufacturing of Mg alloys for biomedical applications: Current status and challenges. Curr. Opin. Biomed 18:100276. https://doi.org/10.1016/j.cobme.2021.100276
[12] Karunakaran R, Ortgies S, Tamayol A, Bobaru F, Sealy MP (2020) Additive manufacturing of magnesium alloys. Bioact. Mater. 5(1):44–54. https://doi.org/10.1016/j.bioactmat.2019.12.004
[13] Liu S, Yang W, Shi X, Li Bin, Duan S, Guo H, Guo J (2019) Influence of laser process parameters on the densification, microstructure, and mechanical properties of a selective laser melted AZ61 magnesium alloy. J. Alloy Compd. 808:151160. https://doi.org/10.1016/j.jallcom.2019.06.261
[14] Niu X, Shen H, Fu J, Yan J, Wang Y (2019) Corrosion behaviour of laser powder bed fused bulk pure magnesium in hank's solution. Corros. Sci. 157:284–294, https://doi.org/10.1016/j.corsci.2019.05.026
[15] Wei K, Zeng X, Wang Z, Deng J, Liu M, Huang G, Yuan X (2019) Selective laser melting of Mg-Zn binary alloys: Effects of Zn content on densification behavior, microstructure, and mechanical property. Mater. Sci. Eng. 756:226-236. https://doi.org/10.1016/j.msea.2019.04.067
[16] Xu, R, Zhao MG, Zhao YC, Liu L, Liu C, Gao C, Shuai C, Atrens A (2019) Improved biodegradation resistance by grain refinement of novel antibacterial ZK30-Cu alloys

produced via selective laser melting. Mater. Lette. 237:253–257. https://doi.org/10.1016/j.matlet.2018.11.071
[17] Zumdick NA, Jauer L, Kersting LC, Kutz TN, Schleifenbaum JH, Zander D (2019) Additive manufactured WE43 magnesium: A comparative study of the microstructure and mechanical properties with those of powder extruded and as-cast WE43. Mater. Charact. 147:384–397. https://doi.org/10.1016/j.matchar.2018.11.011
[18] Li Y, Zhou J, Pavanram P, Leeflang MA, Fockaert LI, Pouran B, Tumer N, Schroder KU, Mol JM, Weinans H, Jahr H, Zadpoor AA (2018) Additively manufactured biodegradable porous magnesium. Acta Biomater 67:378–392. https://doi.org/10.1016/j.actbio.2017.12.008
[19] Somasundaram M, Uttamchand NK, Annamalai AR, Jen CP (2022) Insights on Spark Plasma Sintering of Magnesium Composites: A Review. J. Nanomater. 12(13):2178. https://doi.org/10.3390/nano12132178
[20] Rotem R, Aghion E (2016) Innovative approach to protect magnesium powder during sintering. IJMR 107(6):553–557. https://doi.org/10.3139/146.111373
[21] Wolff M, Ebel T, Dahms (2010) Sintering of Magnesium. Adv. Eng. Mater. 12(9):829–836. https://doi.org/10.1002/adem.201000038
[22] Burke P, Kipouros Gj, Fancelli D, Laverdiere V (2013) Sintering Fundamentals of Magnesium Powders. Can. Metall. Q. 48(2):123–132. https://doi.org/10.1179/cmq.2009.48.2.123
[23] Salehi M, Maleksaeedi S, Nai SML, Meenashisundaram GK, Goh MH, Gupta M (2019) A paradigm shift towards compositionally zero-sum binderless 3D printing of magnesium alloys via capillary-mediated bridging. Acta Mater. 165:294-306. https://doi.org/10.1016/j.actamat.2018.11.061
[24] German RM, Suri P, Park SJ (2009) Review: liquid phase sintering. J. Mater. Sci. 44(1):1–39. http://doi.org/10.1007/s10853-008-3008-0
[25] Johnson JL, German RM (1996) Solid-state contributions to densification during liquid-phase sintering. Metall. Mater. Trans. B. 27(6):901–909. http://doi.org/10.1007/s11663-996-0003-1
[26] Mora CF, Kwan AKH (2020) Sphericity, shape factor, and convexity measurement of coarse aggregate for concrete using digital image processing. Cem. Concr. Res. 30(3):351-358. https://doi.org/10.1016/S0008-8846(99)00259-8
[27] Salehi M, Seet HL, Gupta M, Farnoush H, Maleksaeedi S, Nai MLS (2020) Rapid densification of additive manufactured magnesium alloys via microwave sintering. Addit. Manuf. 37:101655. https://doi.org/10.1016/j.addma.2020.101655
[28] Celikin M et al. (2023) Development of Nagnesium-Strontium/Calcium (Mg-Sr/Ca)-Based Alloys with Improved Sinterability for Next-Generation Biomedical Implants. Paper presented at the 152nd TMS Annual Meeting, San Diego, California, 19-23 March 2023